

Robust Fitting on a Gate Quantum Computer

Frances Fengyi Yang[✉], Michele Sasdelli^{✉*}, and Tat-Jun Chin[✉]

The University of Adelaide, Adelaide SA 5000, Australia
 {fengyi.yang,michele.sasdelli,tat-jun.chin}@adelaide.edu.au

Abstract. Gate quantum computers generate significant interest due to their potential to solve certain difficult problems such as prime factorization in polynomial time. Computer vision researchers have long been attracted to the power of quantum computers. Robust fitting, which is fundamentally important to many computer vision pipelines, has recently been shown to be amenable to gate quantum computing. The previous proposed solution was to compute Boolean influence as a measure of outlyingness using the Bernstein-Vazirani quantum circuit. However, the method assumed a quantum implementation of an ℓ_∞ feasibility test, which has not been demonstrated. In this paper, we take a big stride towards quantum robust fitting: we propose a quantum circuit to solve the ℓ_∞ feasibility test in the 1D case, which allows to demonstrate for the first time quantum robust fitting on a real gate quantum computer, the IonQ Aria. We also show how 1D Boolean influences can be accumulated to compute Boolean influences for higher-dimensional non-linear models, which we experimentally validate on real benchmark datasets.

Keywords: Robust model fitting · Gate quantum computer

1 Introduction

Many computer vision pipelines require estimating a geometric model from noisy and outlier-contaminated data $\mathcal{D} = \{\mathbf{p}_i\}_{i=1}^N$. Consensus maximization [24] is a popular framework for robust fitting in computer vision, where one attempts to find the model \mathbf{x} that agrees with as many of the points as possible, *i.e.*,

$$\underset{\mathbf{x} \in \mathcal{M}}{\text{maximize}} \sum_{i=1}^N \Psi_\epsilon(r_i(\mathbf{x})). \quad (1)$$

Domain $\mathcal{M} \subseteq \mathbb{R}^d$ defines the allowable parameters \mathbf{x} of the model, $r_i : \mathcal{M} \mapsto \mathbb{R}_{\geq 0}$ is the residual of model \mathbf{x} w.r.t. the i -th “point” \mathbf{p}_i , and

$$\Psi_\epsilon(r) = \begin{cases} 1 & \text{if } r \leq \epsilon, \\ 0 & \text{otherwise,} \end{cases} \quad (2)$$

is an indicator function that checks if the size of a residual is less than the user-supplied inlier threshold ϵ . Each \mathbf{x} has a corresponding consensus set

$$\mathcal{I}(\mathbf{x}) = \{i \in \{1, \dots, N\} \mid r_i(\mathbf{x}) \leq \epsilon\}, \quad (3)$$

* Dr. Michele Sasdelli is funded by Centre for Augmented Reasoning (CAR).

i.e., the set of inliers of \mathbf{x} , and (1) is equivalent to finding the \mathbf{x}^* with the largest consensus set $\mathcal{I}(\mathbf{x}^*)$. The equivalent outlier removal interpretation of (1) is

$$\begin{aligned} & \underset{\mathbf{x} \in \mathcal{M}, \mathbf{z} \in \{0,1\}^N}{\text{minimize}} && \|\mathbf{z}\|_1 \\ & \text{subject to} && r_i(\mathbf{x}) \leq \epsilon \text{ if } z_i = 0, \quad i = 1, \dots, N, \end{aligned} \quad (4)$$

where $\mathbf{z} = [z_1, z_2, \dots, z_N]$ is a binary vector selecting a subset of \mathcal{D} as outliers, and the goal is to remove the least number of outliers to find a consensus set.

Arguably the most popular class of methods for (1) are the random sampling techniques (*i.e.*, RANSAC [24] and its variants), which do not provide any guarantees. Indeed, complexity results indicate that consensus maximization is generally intractable and inapproximable [18], and one must resort to exhaustive search to find \mathbf{x}^* (see [66] for a recent survey) or convex relaxation [59] to attempt to find a bounded approximation. Consistent with the theory [18], iterative optimization schemes [15, 32] also do not provide optimality guarantees.

More broadly, the difficulty of consensus maximization reflects the general hardness of robust fitting under different formulations and settings [7, 55]. This has motivated researchers to explore alternative approaches (including machine learning [14, 46, 54, 57]) and computing paradigms to solve the problem.

1.1 Quantum solutions for robust fitting

An active direction has been the development of quantum solutions for robust fitting [19, 21, 23]. Such methods exploit quantum computers to solve robust fitting or appropriate subproblems within a classical optimization framework.

Chin *et al.* [19] proposed to use the Bernstein-Vazirani (BV) quantum circuit to compute Boolean influence, which has proven to be a bona fide measure of outlyingness [52, 53, 64]. The BV circuit allows influence computation to be parallelized across data points, thereby yielding a provable speedup. However, the solution rests upon the assumption that an ℓ_∞ feasibility test has a quantum implementation. While in theory any classically efficient routine has an efficient quantum realization [41, Sec. 3.25], a quantum implementation of the ℓ_∞ test was not provided in [19], thereby precluding real quantum demonstrations.

Doan *et al.* [21] exploited the ability of quantum annealers (QA) to conduct energy minimization to build a hybrid quantum-classical robust fitting algorithm. The key is to rewrite (1) as a hypergraph vertex cover (HVC) problem, which is amenable to quantum annealing. To avoid the exponential growth in the hyperedges, Doan *et al.* iteratively sample the hyperedges (on a classical machine) and solve the resulting HVC instances (on a D-Wave QA) to yield intermediate solutions with error bounds. Farina *et al.* [23] proposed quantum multi-model fitting, where quantum annealing is used to solve disjoint set cover to select the optimal combination of hypotheses that fit the input data.

1.2 Gate quantum computers vs adiabatic quantum computers

Gate quantum computers (GQC) and adiabatic quantum computers (AQC), *aka* QA, are the two major paradigms to realize quantum computers. Briefly, GQC

operates by sequential application of quantum gates to manipulate quantum states encoded in a set of qubits to execute quantum algorithms. On the other hand, AQC follows the adiabatic theorem to gradually evolve a system from an easily prepared initial state to the ground state of a problem Hamiltonian, thereby finding the solution to optimization problems.

GQC is more general than AQC in the sense that the former can implement arbitrary algorithms, potentially with significant speed-ups over the classical counterparts. In fact, some of the most prominent quantum algorithms, *e.g.*, Shor’s algorithm for prime factorization [41, Chap. 5] and Grover’s algorithm for unstructured search [41, Chap. 6], are based on GQC. On the other hand, AQC solves optimization problems in the form of quadratic unconstrained binary optimization (QUBO), hence, the targeted problem needs to be mapped to QUBO form, often by introducing additional variables and hyperparameters. The speed-up achievable by AQC is also more difficult to be ascertained [56].

Since it is still unclear which quantum technology will reach maturity (*e.g.*, realizing a million-qubit system that is robust against noise), it is vital for computer vision researchers to explore both pathways. Indeed, both GQC [19] and AQC [21, 23] have been investigated for robust fitting. However, demonstration of [19] on a GQC is still lacking due to the fundamental gap alluded to above.

1.3 Contributions

This paper bridges the critical gap in [19] by presenting a novel quantum sub-circuit to conduct the ℓ_∞ feasibility test in the BV circuit. Although our solution is limited to 1D problems, it is sufficient to achieve important demonstration of quantum robust fitting on a real GQC, specifically the IonQ Aria [2].

Further, we show how 1D Boolean influence computation can be embedded in a random sampling framework and accumulated to compute higher-dimensional Boolean influence. This enabled us to demonstrate the validity of the computed influences on real benchmark datasets for two-view geometry estimation.

1.4 Shortcomings and outlook

Current gate quantum computers are in the noisy intermediate scale quantum (NISQ) era [9], meaning that the quantum processing units (QPU) contain small number of qubits (tens to low hundreds) and are not sufficiently fault tolerant. This limits the size of input problems and quality of outputs, hence, quantum robust fitting solutions cannot yet outperform established classical methods.

The value of our work lies in exploring an alternative technique that

- is theoretically interesting and can inspire novel classical methods, *e.g.*, [53, 64] (note that *quantum computing* is a subject area at ECCV 2024).
- could become practical in the medium term, given significant investments into building quantum computers, *e.g.*, IBM’s Quantum Roadmap aims to deliver a fully error-corrected system with 200 qubits by 2029 [1].

2 Related work

2.1 Quantum computing in computer vision

Quantum computing has been investigated for diverse applications and problems in computer vision (CV). Larasati *et al.* [31] provide a comprehensive survey on integrating quantum computing techniques within CV, with a particular emphasis on AQC-assisted algorithms. Their survey highlights key applications in robust fitting [21], transformation estimation [26, 37], multiple object tracking (MOT) [63], defect detection in semiconductors [60], and permutation synchronization [12]. Additional contributions to this field include advancements in motion segmentation [4], recognition [38, 44], image classification [13, 17, 39, 40], object detection [33], multi-model fitting [23], matching problems [5, 6, 10, 12, 62], and mesh alignment [6]. All works mentioned above focus on employing AQC by translating problems into an AQC-admissible form, predominantly QUBO.

Furthermore, there is growing interest in exploring GQC for CV tasks. Research in this area, such as robust fitting [19] and point set alignment [42], has laid down a theoretical groundwork, suggesting that quantum-classical hybrid solutions may offer viable paths forward. However, the realization of these concepts in practical quantum implementations has not yet been achieved, with most explorations remaining theoretical or confined to simulations.

2.2 Quantum computing in machine learning

The application of quantum computing to assist learning-based approaches for CV tasks has also received significant attention. This approach represents a shift towards integrating the computational capabilities of quantum computing with conventional learning-based methods in CV. Recent examples of such endeavors are as follows: Rosenhahn and Hirche [47] tackled anomaly detection by proposing to optimise an ordered set of quantum gates to compute a normalizing flow using quantum architecture search (QAS) [68]. This work was inspired by a previous study [34] that formulated a proximity measure to quantify how anomalous a quantum state is. Luo *et al.* [36] implemented a 10-qubit quantum circuit for binary classification employing stochastic gradient descent within Quantum Machine Learning (QML) and Quantum-Assisted Cluster Kernels (QuACK). Furthermore, Silver *et al.* [50] introduced MosaiQ, an enhanced generative adversarial network (GAN) framework, building upon [28], specifically tailored for the generation of high-quality quantum images. The paper details the quantum circuit ansatz for MosaiQ’s generators, which is feasible for execution on contemporary NISQ computers. Training of MosaiQ occurs on a quantum simulator, with inference conducted on both simulator and real QC. [65] proposed an end-to-end quantum-inspired spectral-spatial pyramid network (QSSPN) for hyperspectral image feature extraction and classification.

These initiatives underscore the promising synergy between quantum computing and learning-based strategies, setting the stage for potential advancements in critical optimization challenges inherent to CV.

3 Boolean influence for robust fitting

We first review the concept of Boolean influence for robust fitting [52, 53, 64]. Recall the binary vector $\mathbf{z} \in \{0, 1\}^N$ that represents selection of a subset of \mathcal{D} , *i.e.*, $z_i = 1$ implies that \mathbf{p}_i is in subset \mathbf{z} . The *minimax value* of \mathbf{z} is

$$g(\mathbf{z}) := \min_{\mathbf{x} \in \mathcal{M}} \max_{i=1, \dots, N} z_i r_i(\mathbf{x}) = \min_{\mathbf{x} \in \mathcal{M}} \left\| \begin{bmatrix} z_1 r_1(\mathbf{x}) \\ \vdots \\ z_N r_N(\mathbf{x}) \end{bmatrix} \right\|_{\infty}, \quad (5)$$

i.e., $g(\mathbf{z})$ is the minimum over \mathcal{M} of the maximum residual of points in subset \mathbf{z} . We define the ℓ_{∞} *feasibility test* on \mathbf{z} as

$$f(\mathbf{z}) := \begin{cases} 0 & \text{if } g(\mathbf{z}) \leq \epsilon, \\ 1 & \text{otherwise.} \end{cases} \quad (6)$$

We say that \mathbf{z} is feasible if $f(\mathbf{z}) = 0$ and infeasible otherwise. Intuitively, $f(\mathbf{z}) = 0$ means that there is an \mathbf{x} to which all the points in \mathbf{z} have residuals $\leq \epsilon$, which in the context of robust fitting implies that \mathbf{z} is a consensus set. Conversely, $f(\mathbf{z}) = 1$ implies that \mathbf{z} contains outliers.

Including new points to a subset cannot make the minimax value of the resultant subset smaller, *i.e.*,

$$g(\mathbf{z}_1) \leq g(\mathbf{z}_1 \vee \mathbf{z}_2) \quad (7)$$

where \vee is bit-wise OR. Therefore, f is *monotonic*, *i.e.*,

$$f(\mathbf{z}_1) \leq f(\mathbf{z}_1 \vee \mathbf{z}_2). \quad (8)$$

Employing concepts from monotone Boolean function analysis [43], the Boolean influence (henceforth, just “influence”) of the i -th point under f is

$$\alpha_i = \Pr[f(\mathbf{z}) \neq f(\mathbf{z} \otimes \mathbf{e}_i)] = \frac{1}{2^N} \sum_{\mathbf{z} \in \{0,1\}^N} \mathbb{I}[f(\mathbf{z}) \neq f(\mathbf{z} \otimes \mathbf{e}_i)], \quad (9)$$

where \mathbf{e}_i is the binary vector of all zeros except at the i -th element, \otimes is bit-wise XOR (*i.e.*, $\mathbf{z} \otimes \mathbf{e}_i$ flips the i -th element in \mathbf{z}), and $\mathbb{I}(\cdot)$ returns 1 if the input condition is true and 0 otherwise. Intuitively, α_i is the probability that \mathbf{p}_i will change the feasibility of an arbitrary \mathbf{z} , if \mathbf{p}_i is inserted or removed from \mathbf{z} .

Tennakoon *et al.* [53] and Zhang *et al.* [64] proved that under certain conditions the influences of the inliers in \mathcal{D} are strictly smaller than that of the outliers, which supports using influence as a measure of *outlyingness*.

Example 1 (Robust linear regression). Given N pairs of independent and response measurements $\{(\mathbf{a}_i, b_i)\}_{i=1}^N$ where $\mathbf{a}_i \in \mathbb{R}^d$ and $b_i \in \mathbb{R}$, we wish to estimate the linear relationship $\mathbf{a}^T \mathbf{x} \approx b$ that best fits the data, which is contaminated with outliers. Define the residual of the i -th point $\mathbf{p}_i = (\mathbf{a}_i, b_i)$ as

$$r_i(\mathbf{x}) = |\mathbf{a}_i^T \mathbf{x} - b_i|, \quad (10)$$

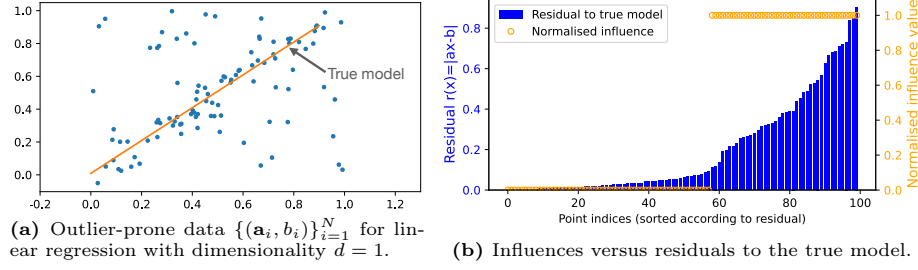


Fig. 1: Influences versus true residuals for robust linear regression. Note that points with lower influence tend to have lower true residuals.

which implies that the minimax problem (5) reduces to linear programming [61]. Fig. 1 plots the normalized influences for an outlier-contaminated data for linear regression versus the residuals $r_i(\mathbf{x}^\circ)$ of the data to the true model \mathbf{x}° . Clearly points with lower influences tend to have lower true residuals.

Example 2 (Fundamental matrix estimation). We aim to find the fund. matrix \mathbf{F} , a homogeneous 3×3 matrix of rank 2, that defines the epipolar equation

$$(\tilde{\mathbf{u}}')^T \mathbf{F} \tilde{\mathbf{u}} = 0 \quad (11)$$

between two views, where $\langle \mathbf{u}, \mathbf{u}' \rangle$ is a point correspondence with $\mathbf{u} = [u \ v]^T$, $\mathbf{u}' = [u' \ v']^T$, and $\tilde{\mathbf{u}} = [\mathbf{u}^T \ 1]^T$. Based on [27, (11.2)], we linearize (11) to

$$[u'u, u'v, u'v', v'u, v'v, v'u, v, u, v, 1] \mathbf{f} = 0, \quad (12)$$

where $\mathbf{f} \in \mathbb{R}^9$ is vectorized \mathbf{F} . Following [27, Sec. 4.1.2], we dehomogenize (12) by fixing the first element of \mathbf{f} to 1, and moving $u'u$ to the RHS to yield

$$[u'v, u'v', v'u, v'v, v'u, v, u, v, 1] \mathbf{x} = -u'u \implies \mathbf{a}\mathbf{x} = b, \quad (13)$$

where $\mathbf{x} \in \mathbb{R}^8$ contains the rest of \mathbf{f} . Given a set of outlier-prone correspondences $\{\langle \mathbf{u}_i, \mathbf{u}'_i \rangle\}_{i=1}^N$, we take $\mathbf{p}_i = (\mathbf{a}_i, b_i)$ following (13), and adopt (10) as the residual. In short, we have converted fundamental matrix estimation into linear regression. Fig. 2 plots the normalized influences for an outlier-contaminated set of correspondences versus the residuals $r_i(\mathbf{x}^\circ)$ of the correspondences to the true model \mathbf{x}° , which was derived from the true fundamental matrix \mathbf{F}° . Evidently points with lower influences have lower true residuals.

Model estimation Given the influences $\{\alpha_i\}_{i=1}^N$, they can be thresholded to yield an inlier set, on which least squares can be applied to estimate \mathcal{M} [19]. More sophisticated heuristics guided by the influences have also been proposed [53, 64].

The viability of influence as an outlying measure on other non-linear estimation problems (*e.g.*, homography estimation, 3D triangulation) has also been established [19, 53, 64]. However, the bottleneck lies in computing the influence (9).

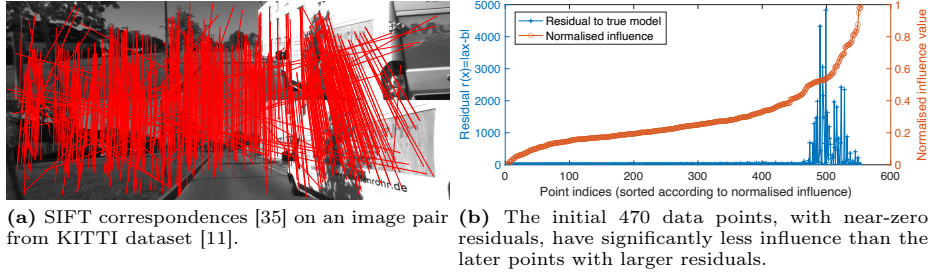


Fig. 2: Influences versus true residuals for a correspondence set for fundamental matrix estimation. Note that points with lower influence tend to have lower true residuals.

4 Quantum algorithm for influence computation

Note that (9) sums over all 2^N combinations of \mathbf{z} . In practice, a finite sample set $Z = \{\mathbf{z}_j\}_{j=1}^M \subset \{0, 1\}^N$ of size M is procured to approximate the influence

$$\hat{\alpha}_i = \frac{1}{M} \sum_{j=1}^M \mathbb{I}[f(\mathbf{z}_j) \neq f(\mathbf{z}_j \otimes \mathbf{e}_i)]. \quad (14)$$

Alg. 1 summarizes the method for influence approximation. Note that Figs. 1 and 2 plot approximate influences for $M = 1000$. It can be shown [19] that $\hat{\alpha}_i$ approaches α_i following the probabilistic bound

$$Pr(|\hat{\alpha}_i - \alpha_i| < \delta) > 1 - 2e^{-2M\delta^2}, \quad (15)$$

where δ is the desired deviation. For example, if $M = 1000$, $Pr(|\hat{\alpha}_i - \alpha_i| < 0.05) > 0.99$, *i.e.*, not many samples are required to achieve a good approximation. However, Alg. 1 can be costly if N is large, *e.g.*, $N > 1000$ points.

4.1 Quantum algorithm

Chin *et al.* [19] proposed a quantum algorithm to speed up (approximate) influence calculation; Alg. 2 summarizes the method. The algorithm employs the BV circuit [8] (shown in Fig. 3), which we briefly describe below; see [19] for details.

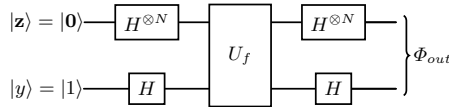


Fig. 3: BV quantum circuit with generic U_f for influence computation.

The adopted BV circuit requires $N + 1$ qubits: the top- N qubits $|\mathbf{z}\rangle$ represent subset selection and the bottom qubit $|y\rangle$ is for auxiliary purposes. The major steps of the BV circuit in the context of Alg. 2 are:

Algorithm 1 Classical method for influence approximation.**Require:** N input data points \mathcal{D} , inlier threshold ϵ , number of iterations M .

```

1: for  $j = 1, \dots, M$  do
2:    $\mathbf{z}_j \leftarrow$  Randomly sample a subset of  $\{1, \dots, N\}$ .
3:   for  $i = 1, \dots, N$  do
4:      $s_{j,i} \leftarrow \mathbb{I}[f(\mathbf{z}_j) \neq f(\mathbf{z}_j \otimes \mathbf{e}_i)]$ .
5:   end for
6: end for
7: for  $i = 1, \dots, N$  do
8:    $\hat{\alpha}_i \leftarrow \frac{1}{M} \sum_{j=1}^M s_{j,i}$ .
9: end for
10: return  $\{\hat{\alpha}_i\}_{i=1}^N$ .

```

Algorithm 2 Quantum method for influence approximation.**Require:** N input data points \mathcal{D} , inlier threshold ϵ , number of iterations M .

```

1: for  $j = 1, \dots, M$  do
2:    $[s_{j,1}, s_{j,2}, \dots, s_{j,N}] \leftarrow$  Run BV circuit with  $\mathcal{D}$  and  $\epsilon$  and measure top- $N$  qubits.
3: end for
4: for  $i = 1, \dots, N$  do
5:    $\hat{\alpha}_i \leftarrow \frac{1}{M} \sum_{j=1}^M s_{j,i}$ .
6: end for
7: return  $\{\hat{\alpha}_i\}_{i=1}^N$ .

```

Initialization Set $|\mathbf{z}\rangle = |\mathbf{0}\rangle$ and $|y\rangle = |1\rangle$, then pass them through Hadamard gates to generate uniform superposition for the top- N qubits

$$|\mathbf{z}\rangle = \frac{1}{\sqrt{2^N}} \sum_{\mathbf{t} \in \{0,1\}^N} |\mathbf{t}\rangle, \quad (16)$$

while the auxiliary qubit is prepared in a state that will facilitate interference.

Oracle function The quantum oracle, represented by gate U_f , implements the feasibility test (6) corresponding to the target problem (more in Sec. 4.2).

Interference After the oracle function, another set of Hadamard gates perform constructive and destructive interference, resulting in the output state

$$\Phi_{out} = \frac{1}{2^N} \sum_{\mathbf{s} \in \{0,1\}^N} \sum_{\mathbf{t} \in \{0,1\}^N} (-1)^{f(\mathbf{t}) + \mathbf{s} \cdot \mathbf{t}} |\mathbf{s}\rangle |1\rangle. \quad (17)$$

Measurement Measure the top- N qubits of Φ_{out} to yield binary string \mathbf{s} .

As outlined in [19, Theorem 1], each element s_i in the measured binary string $\mathbf{s} = [s_1, s_2, \dots, s_N] \in \{0,1\}^N$ is a sample from the Bernoulli distribution

$$Pr(s_i = 1) = \alpha_i. \quad (18)$$

By running the BV circuit M times, Alg. 2 effectively acquires outcomes of the test $\mathbb{I}[f(\mathbf{z}_j) \neq f(\mathbf{z}_j \otimes \mathbf{e}_i)]$ for M samples $\{\mathbf{z}_j\}_{j=1}^M$. Moreover, the sampling is parallelized across the N points by the QPU, thus, Alg. 2 can have a significant computational gain over Alg. 1 if N is large.

4.2 Quantum circuit for ℓ_∞ feasibility test

Kahl and Hartley [29] showed that the ℓ_∞ feasibility test (6) is efficient for quasiconvex residuals (which include the linear case in Examples 1 and 2). Chin *et al.* [19] relied on the fact that any classical computation has a comparably efficient quantum implementation [41, Chap. 3.25] to argue for the existence of U_f , which is responsible for conducting the ℓ_∞ feasibility test on the quantum machine; however, no concrete solution was provided for U_f , which raises doubts of the feasibility of Alg. 2 on a real gate quantum computer.

In this section, we address the critical gap by proposing a quantum circuit for U_f . Although our solution is aimed at the simple 1D “point fitting” problem,

- it is a non-trivial and novel contribution that enables quantum robust fitting to be demonstrated for the first time on a real gate quantum computer.
- the computed influences for point fitting can be accumulated to achieve influence computation for more complex estimation tasks (Sec. 5).

Robust point fitting As alluded to above, our proposed quantum circuit is aimed at robust point fitting, which is a 1D special case of robust linear regression (Example 1) with $d = 1$ and $a_i = 1, \forall i$. The residual reduces to

$$r_i(x) = |x - b_i|, \quad (19)$$

and we aim to find the point $x \in \mathbb{R}$ that is representative (within ϵ) of the inlier population in the data $\mathcal{D} = \{b_i\}_{i=1}^N$. The ℓ_∞ feasibility test (6) reduces to

$$f(\mathbf{z}) = \begin{cases} 0 & \text{if } \max(\{b_i \mid i \text{ s.t. } z_i = 1\}) - \min(\{b_i \mid i \text{ s.t. } z_i = 1\}) \leq 2\epsilon, \\ 1 & \text{otherwise.} \end{cases} \quad (20)$$

Preprocessing We first sort \mathcal{D} decreasingly such that $b_i \geq b_j \forall i < j$. Also, we assume $b_i \geq 0 \forall i$, by offsetting the values as necessary such that $b_N = 0$.

Circuit design The proposed U_f is shown in Fig. 4, with the implementation of subcircuit D shown in Fig. 5. Our design introduces ancillary qubits $|\mathbf{a}\rangle = |\mathbf{a}_1 \mathbf{a}_2\rangle$ and $|\mathbf{v}\rangle = |\mathbf{v}_1 \mathbf{v}_2\rangle$, which are all initialized to $|\mathbf{0}\rangle$. The major circuit blocks are:

- D is the main circuit that computes $f(\mathbf{z})$, while D^{-1} performs “uncomputation” to restore the ancillary qubits as required for U_f in the BV circuit.
- A selects the largest (sorted) number in the subset indicated by $|\mathbf{z}\rangle$. For example, for input $\mathcal{D} = \{7, 5, 3, 2\}$ and $|\mathbf{z}\rangle = |1011\rangle$, applying A yields $|\mathbf{a}_1\rangle = |1000\rangle$, implying the size of $|\mathbf{a}_1\rangle$ being the number of data points N . Block A^{-1} reverses the computation such that $|\mathbf{z}\rangle$ and $|\mathbf{a}_1\rangle$ are restored. Note that following the sequence in Fig. 4, $|\mathbf{z}\rangle$ is in uniform superposition (16) when input to A .
- B selects the smallest (sorted) number in the subset indicated by $|\mathbf{z}\rangle$, *e.g.*, for input $\mathcal{D} = \{7, 5, 3, 2\}$ and $|\mathbf{z}\rangle = |1011\rangle$, applying B yields $|\mathbf{a}_2\rangle = |0001\rangle$.
- V_1 and V_2 encode the numerical values of the input data \mathcal{D} . The number of qubits in $|\mathbf{v}_1\rangle$ and $|\mathbf{v}_2\rangle$ equals the bit precision C of the data. An example data entry to V_1 and V_2 is demonstrated in Fig. 6.

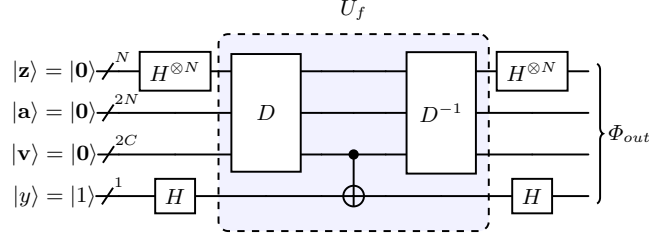


Fig. 4: Proposed quantum gate U_f for point fitting embedded in the BV circuit. The U_f gate introduces auxiliary qubits $|a\rangle$ and $|v\rangle$. The subcircuit D is illustrated in Fig. 5.

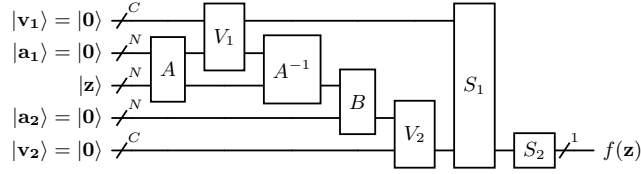


Fig. 5: Composition of subcircuit D from Fig. 4, which includes largest number selector A , smallest number selector B , subcircuits V_1 and V_2 to encode the data values $\{b_i\}_{i=1}^N$, a quantum Fourier transform (QFT) subtractor S_1 [22, 48], and finally a 2ϵ comparator S_2 . $f(\mathbf{z})$ is indicated by the last bit of $|v_2\rangle$. Details of A , B , S_1 , and S_2 are in the supp. material, while an example of V_1 and V_2 is given in Fig. 6.

- S_1 calculates the absolute difference between the values encoded in $|v_1\rangle$ and $|v_2\rangle$ and selected by $|a_1\rangle$ and $|a_2\rangle$. The output is encoded in $|v_2\rangle$. The subtractor [22, 48] is based on Quantum Fourier transform (QFT) [20].
- S_2 takes in $|v_2\rangle$ and calculates its absolute difference with an inbuilt value of 2ϵ , which effectively conducts the feasibility test $f(\mathbf{z})$ (20).

For brevity, we provide the detailed design of the circuits in the supp. material.

Qubit count Denoting N as the number of points and C as the bit precision of the data, the circuit in Fig. 4 consumes $3N + 2C + 1$ qubits. Further optimization is possible to reduce the qubit count—see supplementary material.

5 Influence-based robust fitting of fundamental matrix

Here, we show how influences computed for robust point fitting, which our quantum circuit is specialized for (Sec. 4.2), can be accumulated to obtain influences for more complex robust fitting tasks, specifically fundamental matrix estimation. Alg. 3 summarizes the proposed method. Note that the main goal of Alg. 3 is *enabling validation of the computed and accumulated influences* (Sec. 6.2).

The main idea is conducting RANSAC-style hypothesis sampling (Steps 2–3), evaluate the residual of the input correspondences on each hypothesis (Step 4), then use the residuals as input data for point fitting influence computation (Step 5). The point fitting influences are then accumulated via log averaging (Step 8) to obtain the influences for robust fundamental matrix fitting.

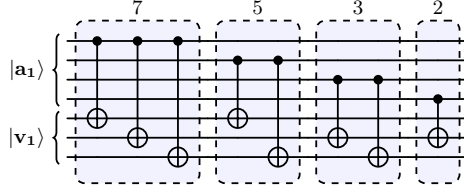


Fig. 6: An example of V_1 that encodes the data $\mathcal{D} = \{7, 5, 3, 2\}$ for point fitting. The number of qubits employed for $|v_1\rangle$ reflects the precision used for the data. The exact same design applies to V_2 , save for changing $|a_1\rangle$ to $|a_2\rangle$ and $|v_1\rangle$ to $|v_2\rangle$.

Algorithm 3 Influence accumulation for fundamental matrix estimation.

Require: Point correspondences $\mathcal{U} = \{\langle \mathbf{u}_i, \mathbf{u}'_i \rangle\}_{i=1}^N$, inlier threshold ϵ , number of hypotheses T , number of iterations M .

- 0: $\mathcal{D} = \{(\mathbf{a}_i, b_i)\}_{i=1}^N \leftarrow$ Linearize the measurements \mathcal{U} (see Example 2).
- 1: **for** $t = 1, \dots, T$ **do**
- 2: $\mathcal{K}_t \leftarrow$ Sample a minimal subset of 8 correspondences from \mathcal{U} .
- 3: $\mathbf{F}_t \leftarrow$ Estimate fundamental matrix from \mathcal{K}_t using 8-point method [27].
- 4: $\{r_i\}_{i=1}^N \leftarrow$ Evaluate linearized residual of \mathcal{D} on \mathbf{F}_t (see Example 2).
- 5: $\{\hat{\alpha}_i^{(t)}\}_{i=1}^N \leftarrow$ Run Alg. 1 or 2 for M iterations with threshold ϵ to compute influences for point fitting problem with residuals $\{r_i\}_{i=1}^N$ as data.
- 6: **end for**
- 7: **for** $i = 1, \dots, N$ **do**
- 8: $\hat{\alpha}_i \leftarrow \frac{1}{T} \sum_{t=1}^T \log(\hat{\alpha}_i^{(t)})$.
- 9: **end for**
- 10: **return** $\{\hat{\alpha}_i\}_{i=1}^N$.

Due to the limitations of current quantum hardware (Sec. 1.4), the number of points N that are feasible for the quantum method (Alg. 2) is restricted (see Sec. 6.1). Thus, to verify Alg. 3, we will mainly use the classical method (Alg. 1).

Model estimation We depart from previous influence-based estimation methods [19, 53, 64]. We first normalize the influences $\{\hat{\alpha}_i\}_{i=1}^N$ to $[0, 1]$. For each γ_h from a uniform sample of thresholds $[\gamma_1, \gamma_2, \dots, \gamma_H] \subset [0, 1]$, we solve

$$\mathbf{x}_h^* = \arg \min_{\mathbf{x} \in \mathcal{M}} \sum_{i=1}^N \mathbb{I}(\hat{\alpha}_i \leq \gamma_h) r_i(\mathbf{x})^2, \quad (21)$$

i.e., least squares fitting on points with influence $\leq \gamma_h$. The model \mathbf{x}_h^* with the highest consensus $\mathcal{I}(\mathbf{x}_h^*)$ is returned as the final robust estimate.

6 Experiments

6.1 Correctness and feasibility of quantum algorithm

Correctness of quantum circuit To validate the proposed quantum algorithm (Sec. 4.2), we used the State Vector Simulator (SV1) on Amazon Braket [3],

which contained 34 qubits. Via the Qiskit framework [45], we implemented the proposed quantum circuit (Fig. 4) with input data $\mathcal{D} = \{7, 5, 3, 2\}$ at $C = 3$ bit precision and $\epsilon = 1$, which consumed 20 qubits (see Sec. 4.2). Fig. 7 plots the computed influences as a function of iteration count M in Alg. 2. It is evident that the computed influences approached the true values $\{0.50, 0.25, 0.25, 0.50\}$ with increasing M . The results indicate the correctness of our circuit and Alg. 2.

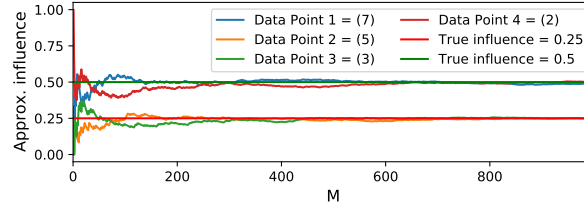


Fig. 7: Approximate influence as a function of iteration count M in Alg. 2, for data $\mathcal{D} = \{7, 5, 3, 2\}$ and $\epsilon = 1$ and implemented on Amazon Braket SV1 quantum simulator.

Feasibility on quantum hardware To demonstrate the feasibility of our proposed quantum algorithm (Sec. 4.2) on a real gate quantum computer, we tested it on IonQ Aria, which is IonQ’s 5th generation trapped-ion quantum computer with 25 physical qubits. The proposed quantum circuit (Fig. 4) with several \mathcal{D} and ϵ (see Tab. 1) were executed on Aria and SV1 for comparison. Due to limited access to the Aria, only $M = 50$ iterations were executed (with reported runtimes of seconds), as compared to $M = 1000$ on SV1.

Tab. 1 shows that the approximate influences from SV1 aligned closely with the true values. On Aria, the approximate influences were close to the true values when the circuit size was small; however, as the circuit size increased, the discrepancy with the true values also increased. This could be due to:

- Insufficient number of iterations M for Alg. 2 on the Aria.
- Lack of error correction on the quantum hardware, which was difficult to implement anyway due to low QPU capacity. Note that the sizes of the larger circuits tested were close to the maximum number of qubits (25).

Nevertheless, the good results from the smaller circuits establish the feasibility of Alg. 2 and the proposed quantum circuit (Fig. 4) on real quantum hardware.

6.2 Influence-based robust fitting of fundamental matrix

We designed an experiment to validate the usefulness of the accumulated influences for a complex robust fitting task. Provided an efficient way to compute influences (e.g. with quantum computing), we showed that competitive CV algorithms can be built. We evaluated the method described in Sec. 5 on the image pairs collected by [11] from the TUM [51], KITTI [25], T&T [30] and CPC [58] datasets. Each collection has 1000 image pairs with views of the same scene and a ground truth fundamental matrix between the views. We used standard established techniques for keypoint extraction (SIFT [35]) and matching proposals [35], returning typically hundreds, up to a few thousands correspondences. The fundamental matrix estimation problem was linearized following

Table 1: Results of Alg. 2 on a real gate quantum computer (IonQ Aria) for $M = 50$ runs and a quantum simulator (Amazon Braket SV1) for $M = 1000$. Legend: N is the number of points, C is the bit precision, \mathcal{D} is input data, nQ is the number of qubits required to implement the quantum circuit (Fig. 4), 2ϵ is twice the inlier threshold, $\{\alpha_i\}_{i=1}^N$ are the true influences, $\{\hat{\alpha}_i^Q\}_{i=1}^N$ are the approx. influence from executing Alg. 2 on IonQ Aria, $\{\hat{\alpha}_i^S\}_{i=1}^N$ are the approx. influence from executing Alg. 2 on SV1.

N	C	\mathcal{D}	nQ	2ϵ	$\{\alpha_i\}_{i=1}^N$	$\{\hat{\alpha}_i^Q\}_{i=1}^N$	$\{\hat{\alpha}_i^S\}_{i=1}^N$
2	1	{0, 1}	9	0	0.50, 0.50	0.50, 0.56	0.51, 0.49
2	1	{0, 1}	9	1	0, 0	0, 0	0, 0
2	2	{0, 2}	11	1	0.50, 0.50	0.50, 0.58	0.50, 0.49
2	3	{2, 4}	13	1	0.50, 0.50	0.46, 0.56	0.51, 0.50
2	3	{2, 4}	13	2	0, 0	0, 0	0, 0
3	3	{2, 4, 7}	16	3	0.50, 0.25, 0.50	0.49, 0.23, 0.53	0.50, 0.26, 0.52
4	3	{2, 3, 5, 7}	19	2	0.50, 0.25, 0.25, 0.50	0.48, 0.39, 0.41, 0.53	0.50, 0.25, 0.25, 0.49

Example 2. We constructed ground truth inliers/outliers labels. For each correspondence we calculated the epipolar lines and thresholded the sum of the two distances between pixels and the lines at 6 pixels to create the labels.

First, the influences for the correspondences were obtained by Alg. 3 together with Alg. 1 for influence computation. As shown by [19], influences can be used to distinguish inliers from outliers. A Receiver Operating Characteristic (ROC) Area Under the Curve (AUC) score was calculated for each image pair. The averages of the score over the datasets are shown in Tab. 2. We report the classification ROC AUC score of a RANSAC estimator and of the influences estimated as in [19]. Interestingly, the new method scored favorably compared to both RANSAC residuals and the original method from [19].

We then focused on testing the capabilities of using influences for fundamental matrix estimation. To calculate the model we used the method summarized by (21) in Sec. 5. For the evaluation of the fundamental matrices we use the Symmetric Geometric Distance (SGD) [67] in pixels between virtual correspondences built with the estimated matrix and the ground truth matrix. We followed [11] and normalise SGD between $[0, 1]$ by the length of the image diagonal $f = 1/\sqrt{(w+h)^2}$ obtaining Normalised SGD (NSGD). The NSGD is a method to measure the distance between the ground truth fundamental matrix and the estimated fundamental matrix. Values close to 0 are optimal. When the estimated fundamental matrix has a NSGD lower than 0.05 it is considered accurate. We evaluated the models with the recall of correctly estimated models ($recall = \frac{\#correct}{\#total}$). The performances are reported in Tab. 3. On the left half of the table we also reported RANSAC and USAC-openCV estimators run on the same set, with the same number of iterations and the same inlier/outlier threshold used with our method for fair comparison. On the right half of the table we collected the results from [11] for easy comparison. Our approach showed that an efficient way of calculating influences can be beneficial for robust fitting.

Hyperparameters In the above fundamental matrix experiments, the hyperparameters for our method (Sec. 5) were set as follows: The threshold of the linearized problem was set to $\epsilon = 0.6$; M was set to 1000; T was set to 1000; and $H = 50$ was the number of influence thresholds tested.

Table 2: Average ROC AUC classification scores of inliers/outliers by RANSAC, influence estimated using Alg. 3, and influence estimated using [19] on the linearized problem. The expectation of a random classifier is 0.5 while a perfect classifier returns 1; hence, higher ROC AUC indicate better performance.

	RANSAC	Influence (Alg. 3)	Influence [19]
TUM	0.71	0.83	0.76
KITTI	0.86	0.94	0.86
T&T	0.72	0.82	0.82
CPC	0.75	0.87	0.85

Table 3: Percentage recall at $\text{SGD} \leq 0.05$ (following [11]). In the first three columns we report results obtained on exactly the same correspondences and number of iterations, making the outcomes directly comparable. For quick reference we also report the corresponding numbers from [11].

	Our method (Sec. 5)	RANSAC	USAC-openCV	Obtained from [11]		
				RANSAC	USAC	CF-RSC
TUM	62.8	60.9	54.0	57.4	56.5	69.3
KITTI	85.4	87.0	83.8	91.7	82.7	92.3
T&T	85.1	77.6	88.1	70.0	78.8	90.7
CPC	50.3	42.0	52.5	29.2	49.7	60.9

6.3 Comparisons against AQC-based quantum robust fitting

Note that the AQC-based robust fitting methods of [21, 23] employed very different problem formulations to ours (see Sec. 1.1). A comparison with our GQC-based method would thus not be a meaningful comparison of quantum robust fitting. Moreover, the amenable problem sizes and solution quality of AQC are also limited [21, 23], thus, conclusions drawn would not be scalable.

7 Conclusions and discussion

We demonstrated for the first time quantum robust fitting on a GQC using a novel quantum circuit for ℓ_∞ feasibility test in point fitting. We also showed how influence, a measure of outlyingness, can be accumulated to obtain influence for more complex estimation tasks. Results on a quantum simulator (Amazon Braket SV1) confirmed the algorithm’s correctness, while tests on a GQC (IonQ Aria) proved its feasibility on real quantum hardware. A fundamental matrix estimation benchmark indicated the promise of our method on a practical task.

Note that Alg. 3 is a hybrid quantum-classical algorithm, similar to [21, 23]. While our method does not provide exponential speed-up to robust fitting, hybrid methods are nevertheless crucial to facilitate adoption of quantum computers in the near term [16]. More broadly, developing quantum solutions for problems with existing classical solutions is a useful endeavor, since it can lead to new insights and techniques [49]. In this spirit, our work represents an early but significant attempt at using GQC for a realistic computer vision problem, aiming to inspire more effective quantum methods for vision.

References

1. IBM Quantum Roadmap. <https://www.ibm.com/roadmaps/quantum/>
2. IonQ Aria. <https://ionq.com/quantum-systems/aria>
3. State vector simulator (SV1). <https://docs.aws.amazon.com/braket/latest/developerguide/braket-simulator-sv1.html>
4. Arrigoni, F., Menapace, W., Benkner, M.S., Ricci, E., Golyanik, V.: Quantum motion segmentation. In: European Conference on Computer Vision. pp. 506–523. Springer (2022)
5. Benkner, M.S., Golyanik, V., Theobalt, C., Moeller, M.: Adiabatic quantum graph matching with permutation matrix constraints. In: 2020 International Conference on 3D Vision (3DV). pp. 583–592. IEEE (2020)
6. Benkner, M.S., Löhner, Z., Golyanik, V., Wunderlich, C., Theobalt, C., Moeller, M.: Q-match: Iterative shape matching via quantum annealing. In: Proceedings of the IEEE/CVF International Conference on Computer Vision. pp. 7586–7596 (2021)
7. Bernholt, T.: Robust estimators are hard to compute. Tech. rep., Technische Universität Dortmund (2005)
8. Bernstein, E., Vazirani, U.: Quantum complexity theory. In: Proceedings of the twenty-fifth annual ACM symposium on Theory of computing. pp. 11–20 (1993)
9. Bharti, K., Cervera-Lierta, A., Kyaw, T.H., Haug, T., Alperin-Lea, S., Anand, A., Degroote, M., Heimonen, H., Kottmann, J.S., Menke, T., et al.: Noisy intermediate-scale quantum algorithms. *Reviews of Modern Physics* **94**(1), 015004 (2022)
10. Bhatia, H., Tretschk, E., Löhner, Z., Benkner, M.S., Moeller, M., Theobalt, C., Golyanik, V.: Ccquantum: Cycle-consistent quantum-hybrid matching of multiple shapes. In: Proceedings of the IEEE/CVF Conference on Computer Vision and Pattern Recognition. pp. 1296–1305 (2023)
11. Bian, J., Wu, Y., Zhao, J., Liu, Y., Zhang, L., Cheng, M., Reid, I.: An evaluation of feature matchers for fundamental matrix estimation. In: 30th British Machine Vision Conference 2019, BMVC 2019, Cardiff, UK, September 9–12, 2019. p. 25. BMVA Press (2019)
12. Birdal, T., Golyanik, V., Theobalt, C., Guibas, L.J.: Quantum permutation synchronization. In: Proceedings of the IEEE/CVF Conference on Computer Vision and Pattern Recognition. pp. 13122–13133 (2021)
13. Boyda, E., Basu, S., Ganguly, S., Michaelis, A., Mukhopadhyay, S., Nemani, R.R.: Deploying a quantum annealing processor to detect tree cover in aerial imagery of california. *PloS one* **12**(2), e0172505 (2017)
14. Brachmann, E., Krull, A., Nowozin, S., Shotton, J., Michel, F., Gumhold, S., Rother, C.: Dsac-differentiable ransac for camera localization. In: Proceedings of the IEEE conference on computer vision and pattern recognition. pp. 6684–6692 (2017)
15. Cai, Z., Chin, T., Le, H., Suter, D.: Deterministic consensus maximization with bi-convex programming. In: Ferrari, V., Hebert, M., Sminchisescu, C., Weiss, Y. (eds.) *Computer Vision - ECCV 2018 - 15th European Conference, Munich, Germany, September 8–14, 2018, Proceedings, Part XII. Lecture Notes in Computer Science*, vol. 11216, pp. 699–714. Springer (2018). https://doi.org/10.1007/978-3-030-01258-8_42
16. Callison, A., Chancellor, N.: Hybrid quantum-classical algorithms in the noisy intermediate-scale quantum era and beyond. *Physical Review A* **106**(1), 010101 (2022)

17. Cavallaro, G., Willsch, D., Willsch, M., Michielsen, K., Riedel, M.: Approaching remote sensing image classification with ensembles of support vector machines on the d-wave quantum annealer. In: IGARSS 2020-2020 IEEE International Geoscience and Remote Sensing Symposium. pp. 1973–1976. IEEE (2020)
18. Chin, T.J., Cai, Z., Neumann, F.: Robust fitting in computer vision: Easy or hard? In: Proceedings of the European Conference on Computer Vision (ECCV). pp. 701–716 (2018)
19. Chin, T.J., Suter, D., Ch'ng, S.F., Quach, J.: Quantum robust fitting. In: Proceedings of the Asian Conference on Computer Vision (2020)
20. Coppersmith, D.: An approximate fourier transform useful in quantum factoring. arXiv preprint quant-ph/0201067 (2002)
21. Doan, A.D., Sasdelli, M., Suter, D., Chin, T.J.: A hybrid quantum-classical algorithm for robust fitting. In: Proceedings of the IEEE/CVF Conference on Computer Vision and Pattern Recognition. pp. 417–427 (2022)
22. Draper, T.G.: Addition on a quantum computer. arXiv preprint quant-ph/0008033 (2000)
23. Farina, M., Magri, L., Menapace, W., Ricci, E., Golyanik, V., Arrigoni, F.: Quantum multi-model fitting. In: Proceedings of the IEEE/CVF Conference on Computer Vision and Pattern Recognition (CVPR). pp. 13640–13649 (June 2023)
24. Fischler, M.A., Bolles, R.C.: Random sample consensus: A paradigm for model fitting with applications to image analysis and automated cartography. Communications of the ACM **24**(6), 381–395 (1981)
25. Geiger, A., Lenz, P., Urtasun, R.: Are we ready for autonomous driving? the kitti vision benchmark suite. In: 2012 IEEE conference on computer vision and pattern recognition. pp. 3354–3361. IEEE (2012)
26. Golyanik, V., Theobalt, C.: A quantum computational approach to correspondence problems on point sets. In: Proceedings of the IEEE/CVF Conference on Computer Vision and Pattern Recognition. pp. 9182–9191 (2020)
27. Hartley, R.I., Zisserman, A.: Multiple View Geometry in Computer Vision. Cambridge University Press, ISBN: 0521540518, second edn. (2004)
28. Huang, H.L., Du, Y., Gong, M., Zhao, Y., Wu, Y., Wang, C., Li, S., Liang, F., Lin, J., Xu, Y., et al.: Experimental quantum generative adversarial networks for image generation. Physical Review Applied **16**(2), 024051 (2021)
29. Kahl, F., Hartley, R.I.: Multiple-view geometry under the l_∞ -norm. IEEE Trans. Pattern Anal. Mach. Intell. **30**(9), 1603–1617 (2008)
30. Knapitsch, A., Park, J., Zhou, Q.Y., Koltun, V.: Tanks and temples: Benchmarking large-scale scene reconstruction. ACM Transactions on Graphics (ToG) **36**(4), 1–13 (2017)
31. Larasati, H.T., Kim, H., et al.: Trends of quantum computing applications to computer vision. In: 2022 International Conference on Platform Technology and Service (PlatCon). pp. 7–12. IEEE (2022)
32. Le, H., Chin, T., Suter, D.: An exact penalty method for locally convergent maximum consensus. In: 2017 IEEE Conference on Computer Vision and Pattern Recognition, CVPR 2017, Honolulu, HI, USA, July 21–26, 2017. pp. 379–387. IEEE Computer Society (2017). <https://doi.org/10.1109/CVPR.2017.48>
33. Li, J., Ghosh, S.: Quantum-soft qubo suppression for accurate object detection. In: European Conference on Computer Vision. pp. 158–173. Springer (2020)
34. Liu, N., Rebentrost, P.: Quantum machine learning for quantum anomaly detection. Physical Review A **97**(4), 042315 (2018)
35. Lowe, D.G.: Distinctive image features from scale-invariant keypoints. Int. J. Comput. Vis. **60**(2), 91–110 (2004)

36. Luo, D., Shen, J., Dangovski, R., Soljagic, M.: Quack: Accelerating gradient-based quantum optimization with koopman operator learning. *Advances in Neural Information Processing Systems* **36** (2024)
37. Meli, N.K., Mannel, F., Lellmann, J.: An iterative quantum approach for transformation estimation from point sets. In: *Proceedings of the IEEE/CVF Conference on Computer Vision and Pattern Recognition*. pp. 529–537 (2022)
38. Neven, H., Denchev, V.S., Rose, G., Macready, W.G.: Qboost: Large scale classifier training with adiabatic quantum optimization. In: *Asian Conference on Machine Learning*. pp. 333–348. PMLR (2012)
39. Nguyen, N.T., Kenyon, G.T.: Image classification using quantum inference on the d-wave 2x. In: *2018 IEEE International Conference on Rebooting Computing (ICRC)*. pp. 1–7. IEEE (2018)
40. Nguyen, N.T., Kenyon, G.T., Yoon, B.: A regression algorithm for accelerated lattice qcd that exploits sparse inference on the d-wave quantum annealer. *Scientific Reports* **10**(1), 10915 (2020)
41. Nielsen, M.A., Chuang, I.L.: *Quantum Computation and Quantum Information: 10th Anniversary Edition*. Cambridge University Press (2010)
42. Noormandipour, M., Wang, H.: Matching point sets with quantum circuit learning. In: *ICASSP 2022-2022 IEEE International Conference on Acoustics, Speech and Signal Processing (ICASSP)*. pp. 8607–8611. IEEE (2022)
43. O’Donnell, R.: *Analysis of Boolean functions*. Cambridge University Press (2014)
44. O’Malley, D., Vesselinov, V.V., Alexandrov, B.S., Alexandrov, L.B.: Nonnegative/binary matrix factorization with a d-wave quantum annealer. *PloS one* **13**(12), e0206653 (2018)
45. Qiskit contributors: Qiskit: An open-source framework for quantum computing (2023). <https://doi.org/10.5281/zenodo.2573505>
46. Ranftl, R., Koltun, V.: Deep fundamental matrix estimation. In: *Proceedings of the European conference on computer vision (ECCV)*. pp. 284–299 (2018)
47. Rosenhahn, B., Hirche, C.: Quantum normalizing flows for anomaly detection. *arXiv preprint arXiv:2402.02866* (2024)
48. Ruiz-Perez, L., Garcia-Escartin, J.C.: Quantum arithmetic with the quantum fourier transform. *Quantum Information Processing* **16**, 1–14 (2017)
49. Shor, P.W.: Why haven’t more quantum algorithms been found? *Journal of the ACM (JACM)* **50**(1), 87–90 (2003)
50. Silver, D., Patel, T., Cutler, W., Ranjan, A., Gandhi, H., Tiwari, D.: Mosaicq: Quantum generative adversarial networks for image generation on nisy computers. In: *Proceedings of the IEEE/CVF International Conference on Computer Vision*. pp. 7030–7039 (2023)
51. Sturm, J., Engelhard, N., Endres, F., Burgard, W., Cremers, D.: A benchmark for the evaluation of rgb-d slam systems. In: *2012 IEEE/RSJ international conference on intelligent robots and systems*. pp. 573–580. IEEE (2012)
52. Suter, D., Tennakoon, R.B., Zhang, E., Chin, T., Bab-Hadiashar, A.: Monotone boolean functions, feasibility/infeasibility, lp-type problems and maxcon. *CoRR abs/2005.05490* (2020)
53. Tennakoon, R., Suter, D., Zhang, E., Chin, T.J., Bab-Hadiashar, A.: Consensus maximisation using influences of monotone boolean functions. In: *Proceedings of the IEEE/CVF Conference on Computer Vision and Pattern Recognition (CVPR)*. pp. 2866–2875 (June 2021)
54. Truong, G., Le, H., Suter, D., Zhang, E., Gilani, S.Z.: Unsupervised learning for robust fitting: A reinforcement learning approach. In: *Proceedings of the IEEE/CVF Conference on Computer Vision and Pattern Recognition*. pp. 10348–10357 (2021)

55. Tzoumas, V., Antonante, P., Carlone, L.: Outlier-robust spatial perception: Hardness, general-purpose algorithms, and guarantees. In: 2019 IEEE/RSJ International Conference on Intelligent Robots and Systems (IROS). pp. 5383–5390. IEEE (2019)
56. Villanueva, A., Najafi, P., Kappen, H.J.: Why adiabatic quantum annealing is unlikely to yield speed-up. *Journal of physics. A, Mathematical and theoretical* **56**(46) (2023)
57. Wang, G., Manhardt, F., Tombari, F., Ji, X.: Gdr-net: Geometry-guided direct regression network for monocular 6d object pose estimation. In: Proceedings of the IEEE/CVF Conference on Computer Vision and Pattern Recognition. pp. 16611–16621 (2021)
58. Wilson, K., Snavely, N.: Robust global translations with 1dsfm. In: Computer Vision–ECCV 2014: 13th European Conference, Zurich, Switzerland, September 6–12, 2014, Proceedings, Part III 13. pp. 61–75. Springer (2014)
59. Yang, H., Carlone, L.: Certifiably optimal outlier-robust geometric perception: Semidefinite relaxations and scalable global optimization. *IEEE TPAMI* (2022)
60. Yang, Y.F., Sun, M.: Semiconductor defect detection by hybrid classical-quantum deep learning. In: Proceedings of the IEEE/CVF Conference on Computer Vision and Pattern Recognition. pp. 2323–2332 (2022)
61. Yu, J., Eriksson, A., Chin, T.J., Suter, D.: An adversarial optimization approach to efficient outlier removal. *Journal of Mathematical Imaging and Vision (JMIV)* **48**(3), 451–466 (2014)
62. Yurtsever, A., Birdal, T., Golyanik, V.: Q-fw: A hybrid classical-quantum frank-wolfe for quadratic binary optimization. In: European Conference on Computer Vision. pp. 352–369. Springer (2022)
63. Zaech, J.N., Liniger, A., Danelljan, M., Dai, D., Van Gool, L.: Adiabatic quantum computing for multi object tracking. In: Proceedings of the IEEE/CVF Conference on Computer Vision and Pattern Recognition. pp. 8811–8822 (2022)
64. Zhang, E., Suter, D., Tennakoon, R., Chin, T.J., Bab-Hadiashar, A., Truong, G., Gilani, S.Z.: Maximum consensus by weighted influences of monotone boolean functions. In: Proceedings of the IEEE/CVF Conference on Computer Vision and Pattern Recognition (CVPR). pp. 8964–8972 (June 2022)
65. Zhang, J., Zhang, Y., Zhou, Y.: Quantum-inspired spectral-spatial pyramid network for hyperspectral image classification. In: Proceedings of the IEEE/CVF Conference on Computer Vision and Pattern Recognition. pp. 9925–9934 (2023)
66. Zhang, X., Peng, L., Xu, W., Kneip, L.: Accelerating globally optimal consensus maximization in geometric vision. *CoRR* **abs/2304.05156** (2023), <https://doi.org/10.48550/arXiv.2304.05156>
67. Zhang, Z.: Determining the epipolar geometry and its uncertainty: A review. *International journal of computer vision* **27**, 161–195 (1998)
68. Zhu, W., Pi, J., Peng, Q.: A brief survey of quantum architecture search. In: Proceedings of the 6th International Conference on Algorithms, Computing and Systems. pp. 1–5 (2022)

A Overview

The supplementary materials provide implementation details on experiments mentioned in Sec. 6.1 in the main paper. Below is a brief overview of what is included in the document:

- Sec. B outlines the specifics of the quantum circuits’ design, including optimisation tricks.
- Sec. C illustrates the way to execute the quantum circuits on both a quantum simulator and an actual quantum computer.

B Circuit design details

This section elaborates on the circuit design details and optimisation strategies not disclosed in the main paper, further extending the Circuit Design discussion in Sec. 4.2 in the main paper. Please consult Fig. 8 for representations of the quantum gates employed within our circuit design. The majority of gates utilized are detailed in [41, Chap. 5.2]. All quantum circuits created for the experiments detailed in Sec. 6.1 adhere to the framework presented in Fig. 4 of the main paper. Therefore, the following subsections will exclusively focus on the implementation of Block *D*, omitting the repetitive components from further illustration. The following subsections will illustrate 3 circuit instances. Sec. B.1 corresponds to the largest scale case discussed in Sec. 6.1 in the main paper, followed by Sec. B.2 and B.3, where smaller instances and case-by-case optimisation are introduced.

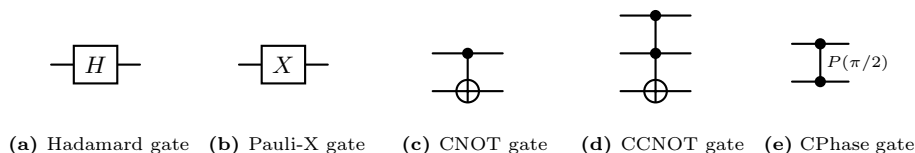


Fig. 8: Quantum gates used in our circuits.

B.1 Circuit Instance 1

This section corresponds to the largest experiment run in Sec. 6.1, where input data $\mathcal{D} = \{7, 5, 3, 2\}$ at $C = 3$ bit precision and $2\epsilon = 2$. Due to the large scale of this particular circuit instance, the implementation of each block in Fig. 5 of the main paper is shown separately in Fig. 9. Please note in this case Block V_1 and V_2 were illustrated in Fig. 6 of the main paper. Instead of using QFT in S_2 , a sequence of controlled-not gates can be used to minimise the circuit depth, at the expense of an additional auxiliary qubit $|b_0\rangle$ to carry the result of the feasibility test.

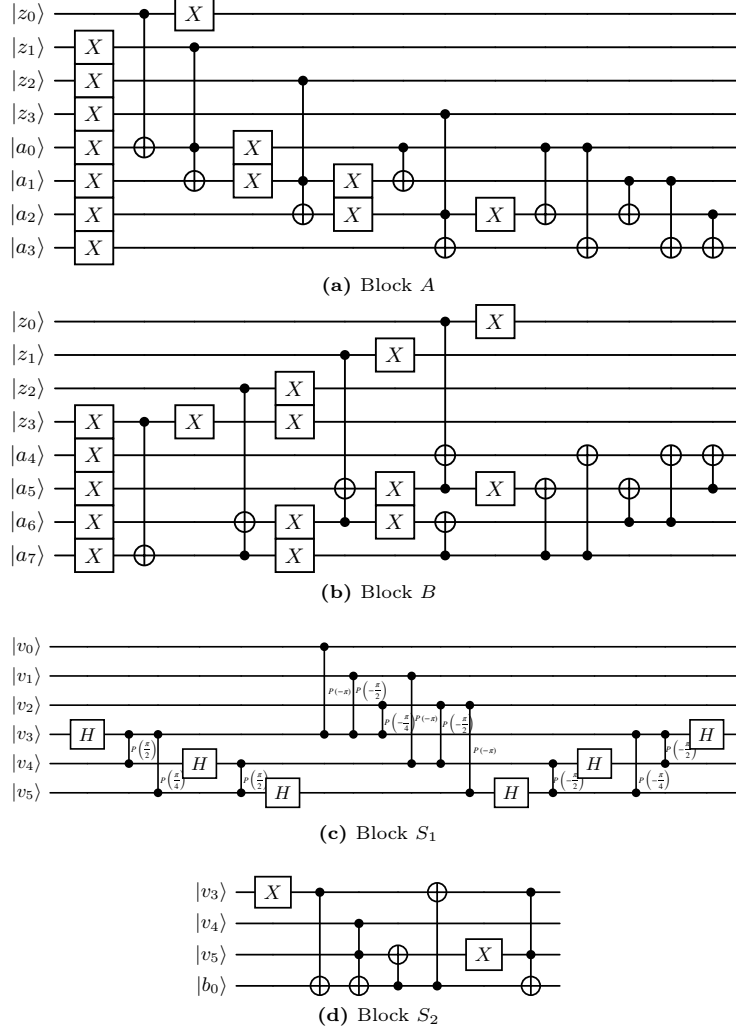


Fig. 9: Each block of Instance 1 is shown separately.

B.2 Circuit Instance 2

This section corresponds to the case where input data $\mathcal{D} = \{1, 0\}$ at $C = 1$ bit precision and $2\epsilon = 0$. See Fig. 10 for the implementation of Block D . In this case, the QFT part in Block S_1 , and the whole block S_2 can be saved, as for S_1 , the difference between the selected data can be computed from a CNOT gate, while for S_2 , the resultant $|v_0\rangle$ from S_1 can be directly passed as the feasibility test outcome.

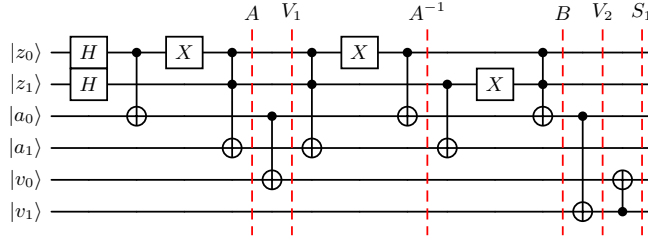


Fig. 10: Instance 2

B.3 Circuit Instance 3

This section corresponds to the case where input data $\mathcal{D} = \{2, 0\}$ at $C = 2$ bit precision and $2\epsilon = 1$. See Fig. 11 for the implementation of Block D . A simple Pauli-X gate is used in S_2 instead of QFT due to the specific computational scenario.

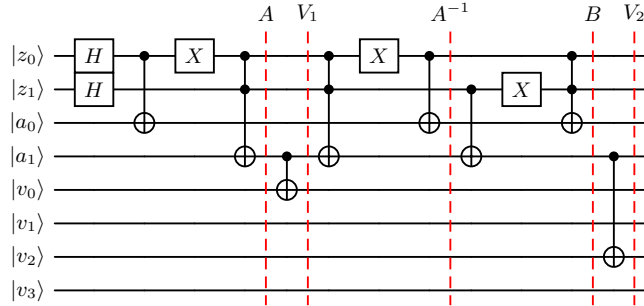
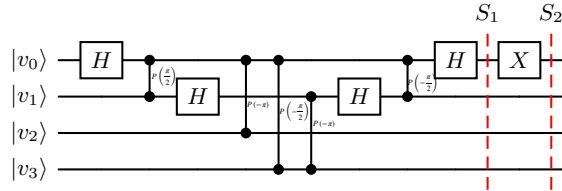
(a) Block A to V_2 of Instance 3.(b) Block S_1 and S_2 of Instance 3.

Fig. 11: Instance 3 split into 2 subplots.

B.4 Input & output explained

In accordance with Fig. 4 and as detailed in Sec. 4.2 of the main paper, the states $|\mathbf{z}\rangle$, $|\mathbf{a}\rangle$, and $|\mathbf{v}\rangle$ are consistently initialized to $|\mathbf{0}\rangle$. The data input occurs through Blocks V_1 and V_2 , as delineated in Fig. 6, where the states of $|\mathbf{v}\rangle$ are

selectively activated via CNOT gates. The focal point of our subsequent analysis is the output associated with $|\mathbf{z}\rangle$. Upon completion, both $|\mathbf{a}\rangle$ and $|\mathbf{v}\rangle$ return to $|0\rangle$, while $|y\rangle$ ends up to be $|1\rangle$.

Considering that $|\mathbf{z}\rangle$ achieves a uniform superposition subsequent to the application of the initial Hadamard gate, the resultant state of $|\mathbf{v}\rangle$ encapsulates the influence sampled across all conceivable subsets of the input dataset. This naturally transits to the way we adopted for result analysis in Sec. 6.1.

C Running quantum circuits

Experiments on our quantum circuits were conducted on both a quantum simulator (SV1) and a real quantum computer (IonQ Aria) via `qiskit_braket_provider` on Amazon Braket. `AWSBraketProvider` facilitates selection among various backends, encompassing both simulators and actual quantum computers. Please refer to code provided for details.